Available online at www.sciencedirect.com
ScienceDirect
Cement and Concrete Research 38 (2008) 300–311
Cement and Concrete Research

Structure of the hydrogen bonds and silica defects in the tetrahedral double chain of xonotlite

Sergey V. Churakov [a,*], Peter Mandaliev [a,b]

[a] Paul Scherrer Institute, Laboratory for Waste Management, CH-5232 Villigen (PSI), Switzerland
[b] Swiss Federal Institute of Technology (ETH), Zürich, Switzerland

Received 18 June 2007; accepted 13 September 2007

Abstract

We use a combined experimental/theoretical approach to investigate the structure and stability of the silicate tetrahedral double chain in xonotlite. The M2a2bc polytype of xonotlite was found to be dominant in the synthetic samples. This polytype was used to predict the relative stability of silica defects in the tetrahedral double chain of xonotlite. The defects in Q^3 sites were found to be substantially more abundant compared to Q^2 tetrahedra. Moreover, the paired substitutions in the silicate double chain at neighbouring Q^3 sites are energetically more stable then isolated Q^3 defects. The defects in the silicate chains of xonotlite offer structural channels accessible for diffusion of ions and water. The defect sites are potential candidates for incorporation of foreign ions in the xonotlite structure. Based on the crystal-chemical similarities with xonotlite the structure of silicate chains in tobermorite and C–S–H phases is discussed.

Keywords: Xonotlite (B); Ab initio simulations (E); Calcium–Silicate–Hydrate (B); Tobermorite (B)

1. Introduction

Among various hydrous calcium silicate hydrates (C–S–H), xonotlite, $Ca_6Si_6O_{17}(OH)_2$, is formed as a by-product of the hardening Portland cement paste. Because of the high thermal stability, special xonotlite rich cements find an application as low density insulating materials [1]. The basic structural element of the xonotlite is the layer of Ca-polyhedra made of three different Ca sites [2]. Two of three Ca sites are seven-coordinated by oxygen while the third one is a distorted octahedron. The silicate tetrahedra form a double chain with *2/m* symmetry, which is formed by condensation of two wollastonite chains (Fig. 1A). The Si tetrahedra can be attached to the Ca layer in two structurally equivalent ways. This results in a number of xonotlite polytypes characterized by different relative arrangement of the silicate double chain in neighbouring Ca layers. The nomenclature of the xonotlite polytypes and their diffraction pattern have been discussed in a previous study [2].

Despite the industrial importance and intensive experimental studies many aspects of xonotlite crystal chemistry are not fully resolved. According to the theoretical stoichiometry the calcium-to-silicon ratio (C/S) in xonotlite is equal to unity. The ideal xonotlite structure should contain only Q^2 and Q^3 type of the Si tetrahedral sites, where $Q^2/Q^3=2$ (in the Q^n notation "*n*" represents the number of bridging oxygen sites per tetrahedron Q) and only one type of OH groups attached to the Ca layer similar to the portlandite structure. High resolution MAS NMR ^{29}Si and ^{1}H spectra of xonotlite [3,4] revealed a minor presence of the Q^1 tetrahedra. ^{1}H MAS NMR spectra of both natural and synthetic samples indicate presence of three different types of proton environments, which can be attributed to Ca–OH, Si–OH linkage and molecular water. The spectral line assigned to Si–OH linkage is more pronounced in synthetic samples and seems to correlate with the amount of the Q^1 tetrahedra [5]. Another study [6] further revealed presence of the Q^1 sites but absence of Si–OH linkage. The existence of terminal Q^1 tetrahedra is a direct evidence for structural defects in the Q^2 or Q^3 sites. The experimental spectra do not allow for unambiguous discrimination of defects between Q^2 and Q^3 tetrahedra. It is also not clear by which mechanism the local charge balance

* Corresponding author. Tel.: +41 56 310 4113; fax: +41 56 310 2821.
E-mail address: sergey.churakov@psi.ch (S.V. Churakov).

0008-8846/$ - see front matter © 2007 Elsevier Ltd. All rights reserved.
doi:10.1016/j.cemconres.2007.09.014

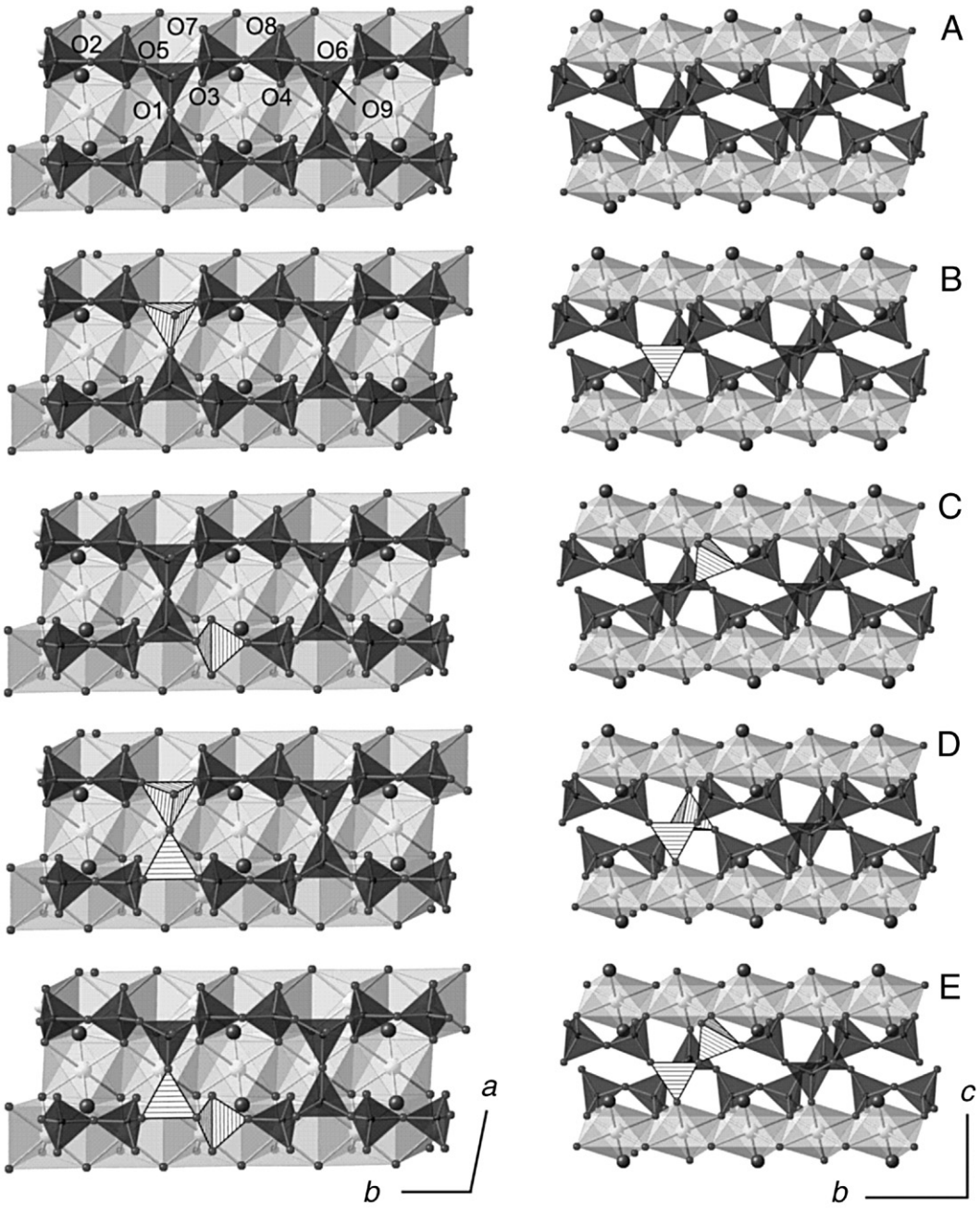

Fig. 1. Fragment of the ideal xonotlite structure (A). Gray octahedral polyhedra enclose Ca atoms. Silicate tetrahedra are black. The oxygen atoms are shown as small black spheres. The oxygen sites of O10H groups are shown as big black spheres. Possible tetrahedral defects in the silica double chain of xonotlite are shown as white hatched polyhedra. Isolated Q^3 (B) and Q^2 (C) sites; coupled Q^3Q^3 (D) and Q^2Q^3 (E) defects.

due to missing Si tetrahedra is satisfied. IR and Raman spectra of natural xonotlite have a strong narrow band at 3620 cm^{-1} accompanied by a broad band in 3200–3500 cm^{-1} range, which is attributed to OH stretching. The commonly observed peak at 1640 cm^{-1} is characteristic for bending in molecular water [7]. Differential thermo-scanning calorimetry and thermo-gravimetric analysis show the main weight loss at 1040 K and 1150 K [8] attributed to OH groups and dehydration of xonotlite into low-T-wollastonite. Minor weight loss observed at 350–370 K is presumably due to loss of molecular water.

The difficulties encountered in the experimental investigations of xonotlite can be overcome using the methods of computational chemistry, which allows the behaviour of the systems to be simulated on the atomic scale. Such methods have been successfully applied to various problems of cement research including investigations of the mechanism of water incorporation in the C–S–H phases [9], isomorphic substitutions of aluminium for silica in the tetrahedral chain [10], the sorption of water and cations on the surface of cement phases [11–14]. The molecular modelling tools can be generally divided in two groups: the empirical force field methods and the

ab initio quantum mechanical calculations, which both inherit advantages and disadvantages. In the ab initio methods the inter-atomic interactions are obtained by solving the electronic Schrödinger equation. Although the quantum mechanical calculations are formally exact and do not require any experimental information on the system, several numerical approximation are used to improve the computational efficiency and can therefore have an effect on the accuracy of the results [15]. Thus the quality of the numerical scheme should be tested against known experimental data. In the empirical force field methods the interatomic interactions are described by model interaction potentials (merely Coulomb and van der Waals forces or harmonic functions for covalent bonds) fitted to reproduce some known experimental data and/or quantum mechanical results. Therefore the structural information on the system of interest or a similar one should be available in advance. In contrast to the computationally expensive ab initio methods that are limited to systems of relatively small size, the empirical force field methods benefit from computational simplicity that opens up the possibility of simulating systems composed of up to 10^6 atoms for several microseconds. Unfortunately, the simple force field parameters are not capable of reproducing the bond breaking events, which include electron transfer or unusual atomistic configurations like defects. In such area the quantum mechanical calculations have an inestimable advantage over the other methods.

In this work we use a coupled experimental–theoretical approach to a shed light upon the unresolved problems of the xonotlite crystallography. Ab initio calculations based on the density functional theory were used to identify the structural positions of the OH groups, the mechanisms of defect formation in the double chain of the silicate tetrahedra and possible incorporation of trace amounts of water in the structure of xonotlite. The theoretical calculations are compared with the results from X-ray diffraction technique (XRD) coupled with Rietveld quantitative phase analysis, scanning electron microscopy (SEM) with energy dispersive microanalysis (EDS), infrared spectroscopy (IR) and thermo-gravimetric analysis on synthetic samples of xonotlite. Further NMR data from the literature are used to discuss the structure of silicate chain in xonotlite.

2. Materials and methods

2.1. Theoretical calculations

All calculations in this work were performed using the density functional theory [16,17] implemented in the CPMD [18] simulation package. The exchange and correlation were taken into account by the generalized gradient approximation BLYP [19,20]. Interaction of the valence electrons with the core states is described by the pseudopotential formalism. We use fully separable norm conserving pseudopotentials generated using the Troullier–Martins scheme [21]. Because of significant overlap of the valence charge density with the core states of Ca atom, the 3s and 3p states were included in the valence. The wavefunctions of valence electrons were expanded into the plane wave basis set up to 70 Ry cut-off energy. The accuracy and transferability of the pseudopotentials as well as the convergence of the plane waves basis set expansion were tested against structure of the simple oxides and hydroxides of Ca and Si as well as their molecules in gas phase. The calculated lattice parameters of the solid phases agree with the experimental values within 1.0–1.5%. The bond distances were reproduced within 1%. The similar set of pseudopotentials for Si, O and H was already used in earlier simulations [22]. The ab initio Car-Parrinello MD simulations in NVE ensemble [23] were performed, with a time step of 0.12 fs and a fictious electron mass of 700 au. In all calculations the supercell contained $2\times2\times2$ unit cells of M2a2bc xonotlite polytype. The geometry of the supercell was fixed at the experimentally determined lattice parameters. A single $k=0$ point in the origin of the Brillouin zone was used in the MD simulations and the geometry optimization. The hydrogen atoms were substituted with deuterium in order to take advantage of the longer integration time step for the equations of motion. Because of the minor influence of the isotopic substitution on the structural properties of solids the deuterium is referred as hydrogen in the discussion, unless the dynamic properties are addressed.

The IR absorption spectrum, $a(\omega)n(\omega)$, of xonotlite was calculated by the Fourier transform of the time correlation function $\langle \mathbf{M}(t)\cdot\mathbf{M}(0)\rangle$, of the total (ionic and electronic) dipole moment of the system according to [24]:

$$a(\omega)n(\omega) = \frac{4\pi\omega\ \tanh\left(\beta\hbar\omega/2\right)}{3\hbar cV} \times \int_{-\infty}^{\infty} \langle \mathbf{M}(t)\cdot\mathbf{M}(0)\rangle e^{-i\varpi t}dt, \tag{1}$$

where $a(\omega)$ is the absorption coefficient, $n(\omega)$ the refractive index, V the volume, $\beta=(k_B T)^{-1}$, T the temperature, k_B the Boltzmann constant, and c the speed of light. In order to get a full spectrum from the Eq. (1) an infinitely long trajectory must be integrated. In practice, the simulations have a finite length that limits the accessible frequency range. The electronic contribution is calculated in the CPMD program using Berry phase scheme [24] and the spectrum was obtained using the maximum entropy method [25]. For characterisation of the IR-bands, we performed a finite difference vibration analyses and calculate the phonon density of state from the dynamics of individual atoms using Fourier transform of the velocity autocorrelation function. Due to the limited simulation time, only the high frequency part of spectra (above 1500 cm^{-1}) was analysed. This part of the spectra includes stretching modes of OH groups only.

For a comparison of the calculated IR bands of deuterium substituted xonotlite with the experimental data, the frequency scale of the calculated spectra must be corrected for the isotope effect and influence of the fictitious electron dynamics on the high frequency vibrations [26]. In a harmonic approximation, the frequency shift due to substitution of hydrogen by deuterium can be expressed by Eq. (2):

$$\nu_H = \sqrt{\frac{M_D}{M_H}}\nu_D \approx 1.4\nu_D, \tag{2}$$

where ν_H, M_H and ν_D, M_D are frequencies and masses of hydrogen and deuterium, respectively. The correction factor (1.05) due to fictitious electron dynamics was obtained as the ratio of the frequencies calculated from the finite difference analysis of optimized structure of xonotlite at zero Kelvin and the vibrational modes obtained in MD simulations.

The structures of the defects in the double chain of Si tetrahedra were predicted by stepwise simulated annealing. The dangling oxygen sites in defects were terminated with OH groups to establish charge neutrality. To obtain optimal orientation of the OH groups short MD-simulation runs (~1 ps) were performed at 400 K. Then the system was annealed to 300 K and equilibrated for ~1 ps. The IR spectra of xonotlite were derived from subsequent 1 ps trajectories using dipole dynamics technique. Such a short simulation time does not provide valuable record of the rearrangement dynamics of hydrogen bonds. Therefore only vibrational dynamics of individual OH groups is discussed, which is adiabatically decoupled from the other dynamical degree of freedom in the system. Once again the systems were annealed to 200 K and equilibrated for ~1 ps. Finally, the systems were cooled down to 0 K and refined using standard geometry optimization methods. The energies of optimized structures were calculated with k-point sampling on 16×16×16 Monkhorst-Pack mesh [27] using the perturbation theory approach [28]. The test calculations indicate that the uncertainties due to k-point mesh are below 0.1 kJ/mol. The energy differences are converged with respect to plane wave basis set within 3 kJ/mol.

2.2. Materials and analytical methods

2.2.1. Sample preparation

The sample of xonotlite was synthesized by mixing stoichiometric quantities of SiO_2 and CaO powder materials (Ca/Si=1.0) with 220 ml argon-purged Milli-Q water [1]. Milli-Q water generated by a Millipore water purification system was used for the preparation of the solutions (Millipore, USA). To prevent CO_2 contamination in the samples, all experiments and handling of the materials were carried out in a glovebox with controlled N_2 atmosphere (CO_2, O_2 <2 ppm, T=290 K+/−3 K). The suspension was placed in 250 ml Teflon Parr bombs and heated in a oven at 490 K for 30 days. The white paste obtained, was dried over saturated $CaCl_2$ solution in a closed container in the glovebox.

2.2.2. SEM/EDS analysis

Scanning electron microscopy (SEM) analysis was conducted at the Laboratory for Material Behaviour (LWV), Paul Scherrer Institut (PSI), using a Zeiss DSM 962 microscope, operated at an accelerating voltage of 20 kV and a beam current of 76 μm. The microscope is equipped with a Si(Li)-detector for energy dispersive microanalysis (EDS). The spot size was ~1×1 μm^2, and the penetration depth was ~6 μm at the used incident beam energy.

2.2.3. Infrared spectroscopy

IR spectra were recorded at the Electrochemistry Laboratory (ECL), Paul Scherrer Institut (PSI), using a Perkin-Elmer System 2000 spectrophotometer. The measurements were conducted in the range 370 cm^{-1}–5000 cm^{-1} at room temperature using KBr pellets, which were prepared by mixing appropriate amounts of KBr and xonotlite, dried at 520 K and 6 hours.

2.2.4. Thermogravimetric analysis (TG/DTA)

Thermogravimetric analysis (TG/DTA) was carried out at the Solar Technology Laboratory, Paul Scherrer Institut (PSI), on a Netzsch STA 409 oven Typ 6.225.6-83 in the range between 300 K and 1350 K. The measurements were conducted in open Al_2O_3 vessels under a argon gas-flow (100 ml/min) at a heating rate of 20 K/min using about 20 mg of powder material.

2.2.5. XRD analysis

The XRD measurements were performed at the Swiss Federal Laboratories for Materials Testing and Research (Empa, Dübendorf). The diffraction pattern used to identify the different xonotlite polytypes present in the synthetic sample was collected using a Philips Xpert diffractometer operating in Bragg-Brentano geometry ($\theta/2\theta$) and using an XCelerator detector module at a nominal pressure. The following conditions were employed: power 40 kV, 40 mA, copper $K\alpha_{1,2}$-radiation (ratio $K\alpha_1/K\alpha_2$ 0.50), divergence slit 0.25°, primary scatter slit 0.76 mm, receiving scatter slit 0.25°, two soller slits, flat-plate sample (round sample holder), specimen: 22 mm (radius)×2 mm (thickness), particle size <63 μm. The scans were taken between 2θ of 5.00° and 2θ of 80° at increments of 2θ 0.017°. The counting time was 60 s for each step. The crystal structure parameters of xonotlite polymorphs and their relative content in the synthetic products were obtained based on Rietveld refinement technique (see Appendix A for details).

3. Results

3.1. Ideal xonotlite structure

3.1.1. Experimental

The hydrothermal synthesis under the given conditions results in white fibrous crystals of xonotlite (Fig. 2). The crystals have diameters from 50 nm to 200 nm and they are 2–8 μm in length. The results of SEM/EDS indicate that the best crystallized samples consist of 17.8% (+/−0.1) Ca and 17.5% (+/−0.1%) Si,

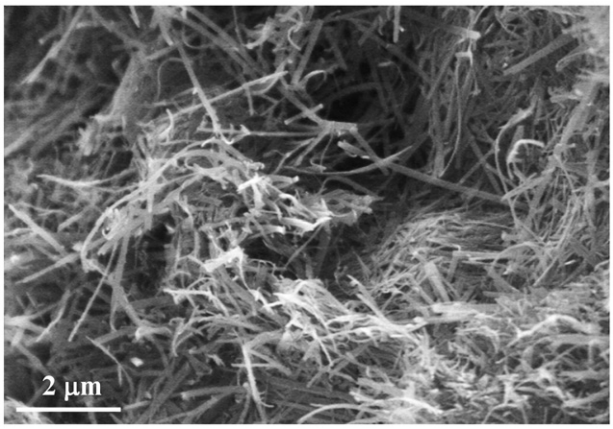

Fig. 2. Scanning electron microscopy image of synthetic xonotlite crystals.

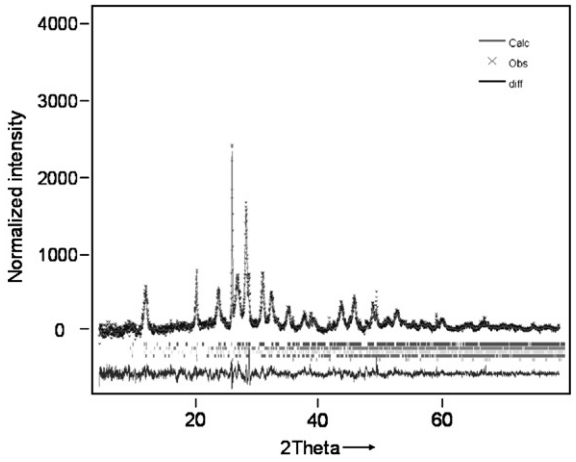

Fig. 3. Rietveld analysis of synthetic xonotlite. The positions of characteristic reflections from individual xonotlite polytypes (M2a2bc, Ma2b2c, Ma2bc, M2a2b2c) and quarz are shown below XRD spectra from top to the bottom, respectivelly.

which corresponds to a C/S ratio of nearly 1.0. For purely crystallized samples the C/S ratio can vary between 1.0 and 1.15. The XRD powder pattern did not indicate the presence of any other phases such as portlandite, calcite or 11.3 Å tobermorite (Fig. 3). The absence of 11.3 Å tobermorite indicates the complete phase transition of 11.3 Å tobermorite to xonotlite. Nevertheless, the high background contribution is an indication for the presence of a small amount of amorphous material. The portion was estimated to be less than 3%. The excess of Ca can not be explained by the presence of additional phases, and therefore should be attributed to the crystal chemistry of xonotlite.

The refined lattice parameters and the relative contribution of the different xonotlite polytypes obtained by quantitative phase analysis using Rietveld refinement are given in Table 1. All four xonotlite polytypes are present. The M2a2bc polytype is the dominant phase under the given reaction conditions. The results of the synthesis are different from the natural samples in which the M2a2b2c polytype is abundant. The difference is likely due to variations in the crystal growth conditions.

3.1.2. Calculations

The positions of atoms in the xonotlite structure were calculated as an average over ab initio MD trajectory on M2a2bc polytype which was found to be dominant in the synthetic samples. The results of the calculations and the experimental data are summarized in Table 2. The calculations are in agreement with the experimental data within 0.01 of the fractional coordinates.

Table 1
Lattice parameter of xonotlite polytypes derived from the synthetic reaction product and published data for natural xonotlite samples

Cell parameters	Synthetic sample (this work)				Natural sample [1]
	M2a2bc	Ma2bc	M2a2b2c	Ma2b2c	
A [Å]	8.69	8.70	17.68	17.14	17.03
B [Å]	7.367	7.35	7.17	7.34	3.67
C [Å]	7.033	13.99	7.05	14.08	7.01
α	89.53	90.46	90.01	90	90
β	89.59	90.29	90.4	90.55	90.33
γ	102.20	102.27	102.27	90	90
Space group	$P\bar{1}$	P 2/a	$A\bar{1}$	A 2/a	P 2/a
Single polytypes fraction [%]	34.66	15.61	4.99	33.12	

Table 2
Average atomic position in xonotlite obtained by ab initio simulations and experimental XRD data [3]

	Calculated (this work)			Hejny and Armbruster [2]		
	x	*y*	*z*	*x*	*y*	*z*
Ca1	0.50	0.50	0.50	0.5000	0.5000	0.5000
Ca2	0.50	0.00	0.50	0.5000	0.0000	0.5000
Ca3	0.13	0.16	0.34	0.1335	0.1645	0.3368
Ca4	0.14	0.66	0.34	0.1385	0.6537	0.3414
Si1	0.21	0.22	0.77	0.2118	0.2170	0.7682
Si2	0.21	0.64	0.77	0.2118	0.6389	0.7686
Si3	0.32	0.96	0.06	0.3182	0.9547	0.0562
O1	0.50	0.00	0.00	0.5000	0.0000	0.0000
O2	0.22	0.43	0.85	0.2190	0.4303	0.8422
O3	0.35	0.71	0.62	0.3512	0.7179	0.6192
O4	0.35	0.21	0.63	0.3434	0.2059	0.6174
O5	0.22	0.11	0.98	0.2297	0.1116	0.9720
O6	0.23	0.75	0.98	0.2294	0.7538	0.9716
O7	0.04	0.64	0.67	0.0424	0.6382	0.6652
O8	0.04	0.14	0.67	0.0463	0.1339	0.6740
O9	0.30	0.95	0.29	0.2988	0.9506	0.2780
O10	0.30	0.45	0.27	0.2977	0.4481	0.2694
D	0.32	0.45	0.14			

"D" stands for deuterium.

3.2. Crystallographic position of hydrogen atoms and the structure of hydrogen bonds

Based on extended bond-valence sum calculations the protons in the structure of xonotlite are assigned to the O10 oxygen sites [29,30]. The exact position of protons and the geometry of the hydrogen bonds have not been determined by analytical techniques. The position of hydrogen atoms (the calculations were performed using mass of deuterium, see Section 2.1 for details) averaged over molecular dynamic trajectory is given in Table 2. The hydrogen–oxygen pair distribution function is shown in Fig. 4 up to 3.5 Å. As expected the protons are bonded

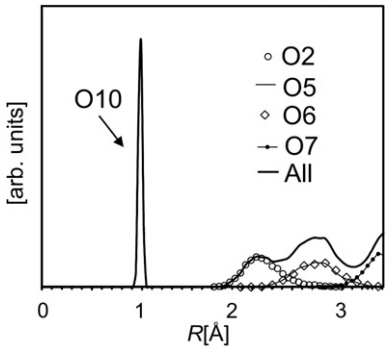

Fig. 4. Hydrogen–oxygen pair distribution in the structure of xonotlite obtained by ab initio molecular dynamics at 300 K. Notation of oxygen sites is given in Fig. 1A.

to the O10 sites and form hydrogen bond to the O2 sites. The O10–H and H...O2 contacts are 0.984 and 2.217 Å, respectively.The average interatomic distances indicate that only O2 site should have measurable influence on the vibrational dynamics of the O10H bond. The distances to O5 and O6 sites are, on average, too long to have any measurable effect on the O10H vibrations. This is consistent with a single sharp absorption line in the IR and Raman spectra commonly reported for xonotlite [7]. The calculated IR spectrum (Eq. (1)) is compared with the experimental measurements in Fig. 5B. After correction for the isotopic shift, see Eq. (2), and the fictitious electronic dynamics (see Section 2.1 for details) the calculated IR spectrum is consistent with the experimental data, as further discussed in the Section 4.2.

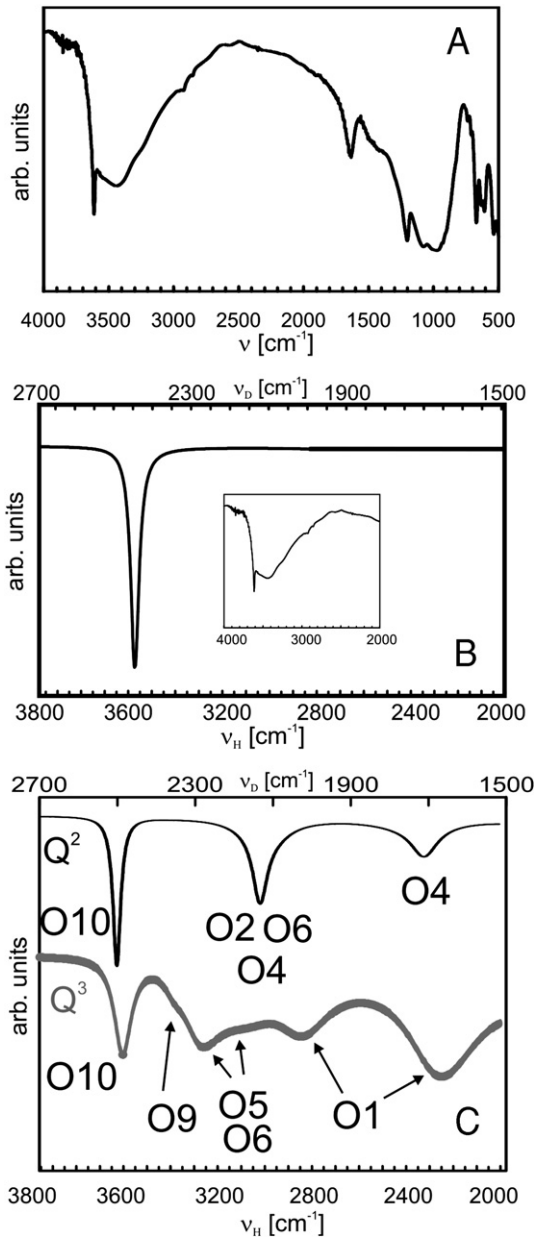

Fig. 5. The measured (A) and calculated IR absorption spectra of the ideal (B) and defected (C) deuterium-xonotlite structure. The bottom axis in the calculated spectra shows the frequency scale corrected for the isotopic substitution of the deuterium by hydrogen and the fictitious dynamics of electrons (the original frequencies of the deuterium xonotlite are shown on the top axis, see text for details). The insert in B shows the fragment of measured IR spectra in the range of frequencies corresponding to ab initio simulations.

3.3. Structure of defects in silicate double chain of xonotlite

The Ca/Si ratio of idealized xonotlite is exactly equal to 1.0. The natural and the synthetic samples differ from the ideal Ca/Si ratio [1]. Increasing deviations from the ideal Ca/Si ratio indicates an increasing degree of disorder in the xonotlite samples. The deficiency of Si in xonotlite can be explained by defects in the chain of Si tetrahedra. The structure of such defects and the mechanism of the charge balancing are still under debates. Presence of M^{3+} or M^{4+} cations in our samples, which could take the structural position of the Si atoms in the double chain, can be excluded by EDS analysis. It is also unlikely that Ca^{2+} atoms occupy Si^{4+} positions in an isolated tetrahedral site. Therefore, we assume in the calculations that the charge compensation is fulfilled by the hydrogarnet substitution mechanism expressed in terms of the Kröger-Vink notation for point defects [31] by:

$$\{\mathrm{Si}\}^{\times}_{\mathrm{Si}} + 2\mathrm{H_2O} = \{\mathrm{H_4}\}^{\times}_{\mathrm{Si}} + \mathrm{SiO_2}, \tag{3}$$

This assumption is consistent with the presence of the second type of OH groups commonly observed in NMR studies [3] and additional broad OH stretching band in IR spectra of xonotlite (Fig. 5A). Ab initio crystal structure optimizations enable us to predict the distribution of protons in the tetrahedral sites and the relative energies of defects formation. Although the composition of the defect is constrained by Eq. (3) the ab initio method allows for bond breaking and bond forming, and in contrast to the empirical simulations, does not require a priori knowledge of the OH connectivity. The structural arrangement of protons in the defect is determined by the requirement of the global energy minimum.

The silicate double chain is built by two "paired" Q^2 tetrahedra (Si1, Si3) and one Q^3 site (Si2) [5]. Although the two different Q^2 sites are present, the geometry of the Si1 and Si3 tetrahedra is very similar. The accuracy of the calculation is not sufficient to discriminate the energy difference between the defects in the Si1 and Si3 sites. Therefore, we arbitrary have chosen a Si3 tetrahedra to be representative for both Si1 and Si3 positions in Q^2 site. Thus, two principally different isolated defects, $\{\mathrm{H_4}\}^{\times}_{Q^3}$ and $\{\mathrm{H_4}\}^{\times}_{Q^2}$ are possible as schematically shown in Fig. 1B and C, respectively.

According to the calculations, the static energy of the defect in $\{\mathrm{H_4}\}^{\times}_{Q^3}$ site is lower by 25.79 kJ/mol than in the $\{\mathrm{H_4}\}^{\times}_{Q^2}$ site. The $\{\mathrm{H_4}\}^{\times}_{Q^3}$ defects should therefore significantly prevail over $\{\mathrm{H_4}\}^{\times}_{Q^2}$ ones:

$$\frac{\{\mathrm{H_4}\}^{\times}_{Q^2}}{\{\mathrm{H_4}\}^{\times}_{Q^3}} = \frac{N_{Q^2}}{N_{Q^3}} e^{-\frac{\Delta E}{RT}} = 2e^{-\frac{\Delta E}{RT}}, \tag{4}$$

where N_{Q^3} and N_{Q^2} are the total amount of Q^3 and Q^2 sites, T is the temperature, R is the gas constant and ΔE is the energy

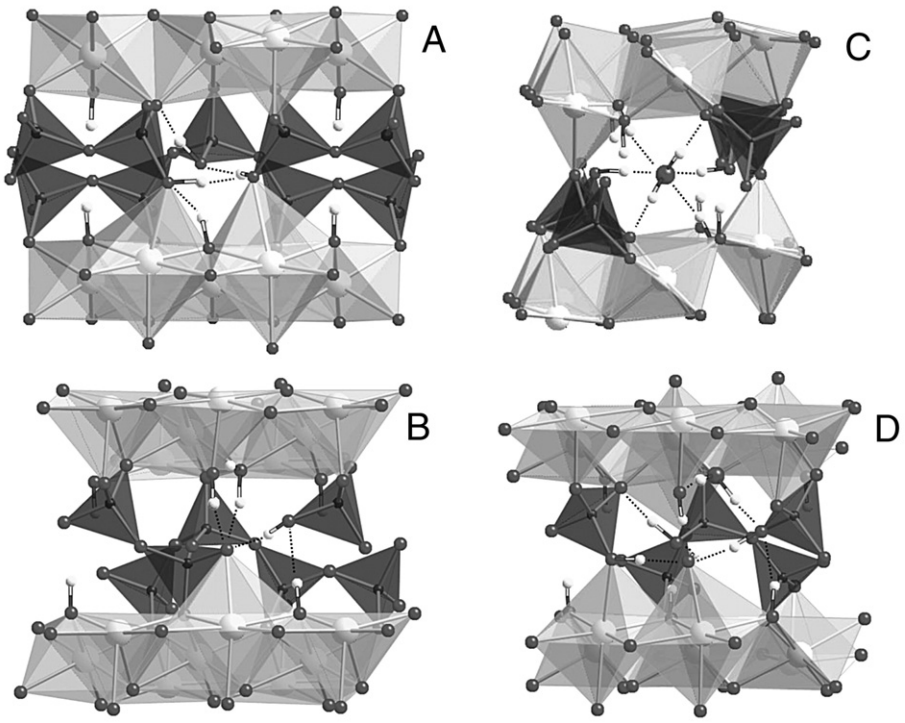

Fig. 6. Optimized structures of the defects in the tetrahedral silicate chain of xonotlite: $\{H_4\}^{\times}_{Q^3}$ (A), $\{H_4\}^{\times}_{Q^2}$ (B), $\{H_8\}^{\times}_{Q^3,Q^3}$ (C), $\{H_8\}^{\times}_{Q^2,Q^3}$ (D) See Fig. 1 for the colour legend. The OH groups are shown as sticks terminated by small bright spheres.

difference between structures with $\{H_4\}^{\times}_{Q^2}$ and $\{H_4\}^{\times}_{Q^3}$ defects. At room temperature (300 K), the ratio $\frac{\{H_4\}^{\times}_{Q^2}}{\{H_4\}^{\times}_{Q^3}}$ is negligibly small 6.4×10^{-5}. At the upper limit of stability of C–S–H phases (500 K) the ratio is equal to 4.0×10^{-3}. The volumetric and entropic contributions to the Gibbs free energy of defects formation are neglected in Eq. (4). It should be noted that the thermal contribution to the free energy difference is small, i.e. order of 1 kJ/mol. The volumetric contribution is unknown but usually negligible at atmospheric pressure.

Table 3
Structure of the hydrogen bonds in the tetrahedral defects of xonotlite

	OH [Å]	H...O [Å]	Angle [°]
$\{H_4\}^{\times}_{Q^3}$			
O9H...O1	0.986	1.768	169.8
O5H...O1	1.001	1.800	156.0
O6H...O5	1.006	1.651	169.5
O1H...O3	1.050	1.560	170.9
$\{H_4\}^{\times}_{Q^2}$			
O4H...O8	1.018	1.703	162.9
O4H...O5	1.014	1.702	151.8
O8H...O5	0.990	2.051	159.9
O2H...O5	1.008	1.612	162.9
H′O4H″			96.7
$\{H_8\}^{\times}_{Q^3,Q^3}$			
O5H...O6	1.006	1.665	170.2
O6H...O1H$_2$	0.994	1.910	154.1
O3...HO1H...O4	1.028	1.656	165.3
O9-H...O1H$_2$	0.982	1.861	165.0
H′O1H″			110.4
$\{H_8\}^{\times}_{Q^2,Q^3}$			
O2H...O6	1.029	1.613	155.2
O6H...O1	0.985	2.457	155.0
O3H...O2	1.001	1.750	144.0
O3H...O7	1.029	1.648	171.1
H′O3H			98.4
O5H...O6	1.021	1.685	172.9
O9H...O1	0.990	1.724	172.2
O1H...O4	1.033	1.616	172.8
O7H...O6	1.018	1.623	174.0

The structural arrangement of OH groups and hydrogen bonds in $\{H_4\}^{\times}_{Q^3}$ and $\{H_4\}^{\times}_{Q^2}$ defects is shown in Fig. 6A and B, respectively. The parameters of hydrogen bonds are summarized in Table 3. The OH-pair distribution functions are presented in Fig. 7. In the energetically favourable $\{H_4\}^{\times}_{Q^3}$ defects the protons are attached to the oxygen sites of the defect tetrahedra. Two chains of hydrogen bonds ≡O6H...O5H...O1H...O3≡ and O9H...O1 are formed. The protonated O9 sites become structurally similar to ≡Ca_3–OH groups in portlandite. The other OH groups form ≡Si–OH linkage on the Q^1 sites. The hydrogen bonds in the defects are significantly shorter than the common O10H...O bonds in xonotlite. We can therefore expect that the vibrational frequencies of the OH in the Si defects should be red-shifted. In Fig. 5C the calculated IR spectrum of xonotlite with defects in $\{H_4\}^{\times}_{Q^3}$ tetrahedra is shown. The vibrational density of states of OD dipoles is given in Fig. 8. The high frequency peak at (~2450 cm^{-1}) can be assigned to O10D...O2 bond. Several broad maxima at lower frequencies can be assigned to the O10D...O2 vibrations in defects based on the vibrational density of states shown in Fig. 8.

In $\{H_4\}^{\times}_{Q^2}$ defects (Table 3) O5 sites remain de-protonated and act as a strong hydrogen bond acceptor (O4H...O5, O2H...O5, O8H...O5). The O4 sites become doubly protonated and the configuration resemble that of a water molecule strongly sorbed on the Ca layer.

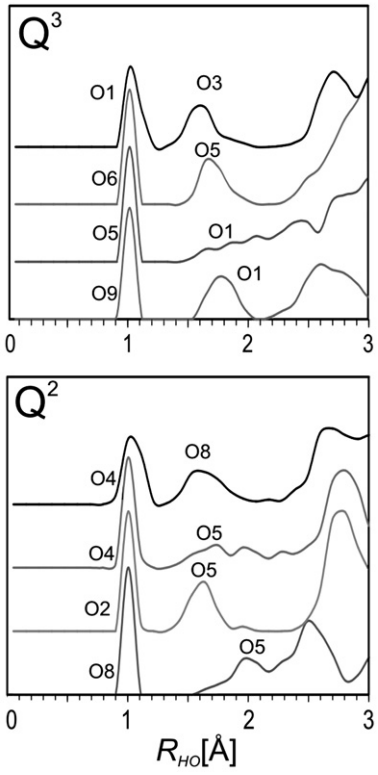

Fig. 7. Hydrogen oxygen pair distribution function for the isolated defects in Q^2 and Q^3 sites.

Considering the geometry of $\{H_4\}^{\times}_{Q^3}$ defects as initial step for subsequent dissolution of the tetrahedral chain we calculate the static energy of coupled defects in the neighbouring silica tetrahedra. Two defect geometries are possible: a coupled substitution in adjacent Q^3 sites $\{H_8\}^{\times}_{Q^3,Q^3}$ (Fig. 1D) and that in neighbouring

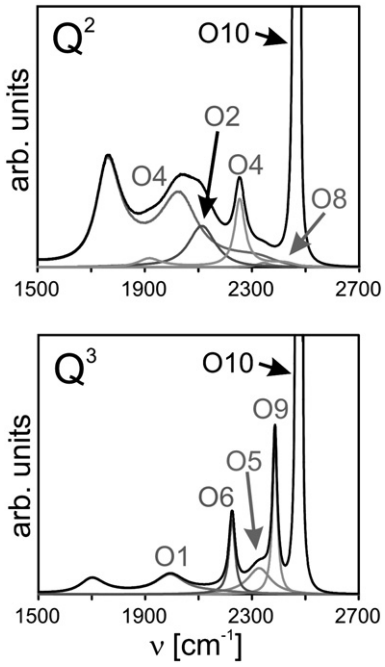

Fig. 8. Calculated vibrational density of states of the OH groups in Q^2 and Q^3 defects.

Table 4
The relative total energy (E_{Total}) of defect formation in the silica double chain of xonotlite for isolated and coupled defects

	E_{Total} [kJ mol^{-1}]	E_{Γ} [kJ mol^{-1}]	E_{Pert} [kJ mol^{-1}]
$\Delta E\ [\{H_4\}^{\times}_{Q_2}-\{H_4\}^{\times}_{Q_3}]$	25.79	25.77	0.02
$\Delta E\ [\{H_8\}^{\times}_{Q_2,Q_3}-\{H_8\}^{\times}_{Q_3,Q_3}]$	40.06	40.09	−0.03
$\Delta E\ [2\{H_4\}^{\times}_{Q_2}-\{H_8\}^{\times}_{Q_3,Q_2}]$	4.97	4.84	0.13

The defect formation in Q^3 sites is energetically favourable compared to Q^2 tetrahedra. Coupled substitution in the neighbouring sites is favourable compared to the two independent substitutions on Q^3 tetrahedra. To illustrate the accuracy of calculations, the single gamma point and k-point sampling contributions to the total energy are given as E_{Γ} and E_{Pert} respectively.

Q^2–Q^3 pair $\{H_8\}^{\times}_{Q^2,Q^3}$ (Fig. 1E). Optimal arrangement of OH groups and hydrogen bonds in $\{H_8\}^{x}_{Q^3,Q^3}$ and $\{H_8\}^{x}_{Q^2,Q^3}$ defects are shown in Fig. 6D and E, respectively. The parameters of hydrogen bonds are summarized in Table 3. The energy of the $\{H_8\}^{\times}_{Q^3,Q^3}$ defect is 40.06 kJ/mol lower than that of the $\{H_8\}^{\times}_{Q^2,Q^3}$ substitution. The energy of the double defect $\{H_8\}^{\times}_{Q^3,Q^3}$ is lower by 4.79 kJ/mol compared to two independent $\{H_4\}^{\times}_{Q^3}$ substitutions (Table 4).

Because the Q^2 defects are very few it is reasonable to assume, for simplicity of the discussion, that isolated defects are formed exclusively in the Q^3 sites. Such assumption should hold up to very high concentration of defects until almost all available Q^3 sites have been consumed. Although the obtained energy difference is close to the accuracy of calculations, the relative abundance of $\{H_4\}^{\times}_{Q^3}$ and $\{H_8\}^{\times}_{Q^3,Q^3}$ can be still calculated from the reaction:

$$2\{H_4\}^{\times}_{Q_3}\{Si\}^{\times}_{Q_3} = \{Si_2\}^{\times}_{Q_3,Q_3} + \{H_8\}^{\times}_{Q_3,Q_3}, \quad (5)$$

$$\frac{\left[\{Si_2\}^{\times}_{Q^3,Q^3}\right]\left[\{H_8\}^{\times}_{Q^3,Q^3}\right]}{\left[\{H_4\}^{\times}_{Q^3}\{Si\}^{\times}_{Q^3}\right]^2} = \exp\left[-\frac{\Delta E}{RT}\right], \quad (6)$$

where $\{Si_2\}^{\times}_{Q^3,Q^3}$ is the concentration of undisturbed Q^3 pairs, $\{H_8\}^{\times}_{Q^3,Q^3}$ is the coupled defect in neighbouring Q^3 sites and

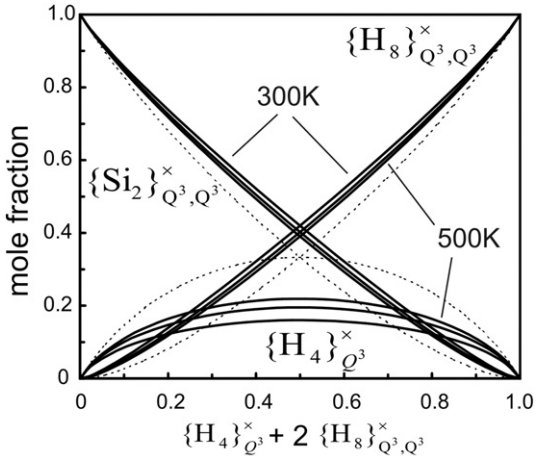

Fig. 9. The equilibrium distribution of doubly substituted Q^3 sites $\{H_8\}^{\times}_{Q^3,Q^3}$, isolated defects $\{H_4\}^{\times}_{Q^3}$ and undisturbed tetrahedral pairs $\{Si_2\}^{\times}_{Q^3,Q^3}$ as function of total concentration of Q^3 substitutions for 300, 400 and 500 K (solid lines). The dotted line shows the ideal solution behaviour (ΔE=0 in Eq. (6)).

$\{H_4\}^{\times}_{Q^3}\{Si\}^{\times}_{Q^3}$ is the Q^3 pair with a single substitution. Eq. (6) neglects the volume change upon defect formation. The volume contribution to the relative stability of defects in Eq. (5) is expected to shift equilibria to the right site, so that $\Delta E >= \Delta E + P\Delta V = \Delta H$. The equilibrium distribution of coupled and isolated defects calculated with Eq. (6) is shown in Fig. 9 as a function of the total fraction of Q^3 substitutions. The diagram clearly illustrates that due to the lower formation energy the double defect substitution becomes more abundant compared to isolated Q^3.

3.4. TG/DTA and IR measurements

The IR spectrum of the best crystallized samples of xonotlite is shown in Fig. 5A. In the range of OH stretching frequencies, the spectrum has a sharp absorption peak at 3611 cm^{-1} and a broad absorption band at ~3430 cm^{-1}. The pronounced absorption peak at 1640 cm^{-1} corresponds to the bending frequency of molecular water. A number of overlapping bands in 500–1500 cm^{-1} range are attributed to the couples stretching and bending of Si tetrahedra and Ca octahedra.

Main weight lost during TG/DTA measurements take place at 1040–1150 K. At this temperature the OH hydrogens are released and the xonotlite transforms to low temperature wollastonite. The small weight loss of about 0.8 wt.% during TG/DTA measurements observed at 350–370 K can be also assigned to the loss of molecular water (Fig. 10). Unexpectedly, the IR band of molecular water and TG/DTA loss at 370 K do not disappear completely after long drying of samples at 520 K.

Based on this, for the first glance contradictory observation, we argue that the larger portion of detected water should be classified as surface absorbed and rather then structurally incorporated. The drying of the probe at 520 K guarantees the release of molecular water from the samples. It is therefore most probably that the dried samples immediately absorb water from the air on the surface during samples preparation for IR and TG/DTA measurements. The kinetics of the water incorporation, on the other hand is slow enough to get the crystalline water during the time of TG/DTA and IR measurements. The C–S–H phases

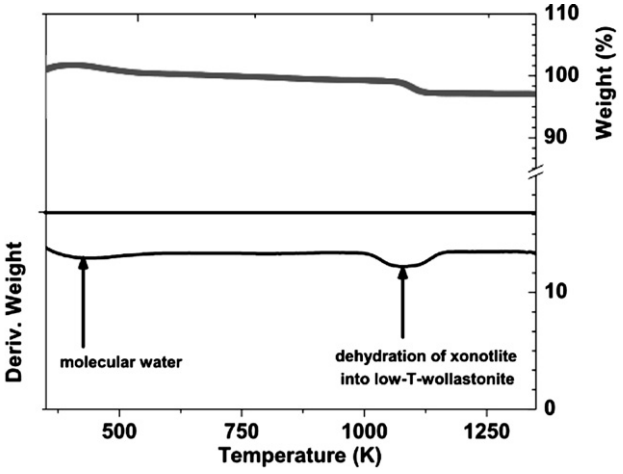

Fig. 10. TG/DTA scan for synthetic xonotlite obtained in the range between 300 K and 1350 K at a constant heating rate.

are known to have strongly hydrophilic surface characteristic [32,33]. Thus we may rule out significant presence of the structurally incorporated water in dried samples. The study of [3] suggest, that vacuum drying and additional measurement, presumably under vacuum, may allow water sorption on the surface of synthetic xonotlite to be excluded.

4. Discussion

4.1. Nature and formation of tetrahedral defects in xonotlite

Although the theoretical xonotlite structure contains only Q^3 and Q^2 tetrahedra, NMR studies detect significant amount of Q^1 sites, indicating the presence of tetrahedral defects in disordered samples. Our calculations suggest that such defects are formed almost exclusively in the Q^3 sites. Additionally, the coupled defects in Q^3 are dominant down to rather low total concentration of Q^3 defects (Fig. 9). These results further support the two stage mechanism of xonotlite formation early proposed by Moorehead [34] and later confirmed by Shaw et al. [8], using in situ X ray diffraction technique. According to this concept, the crystalline phase domains with good periodicity parallel to the *ab* plane and less ordered in the (001) direction are initially formed. In this step the reaction products are similar to C–S–H gel. In the second step, ordering on the structure in c-direction leads to formation of xonotlite crystals. The ordering stage is likely to reflect inclusion of the missing silicate tetrahedra into the silicate chains.

Based on the defect formation energy, we can argue that at the first stage of the xonotlite growth, the two dimensional domains of Ca layers contain only short chains of Q^2 silicate tetrahedra with numerous defects at Q^3 sites. Absence of Q^3 sites in the structure offer channels in the direction of *b* axis (Fig. 6C), which could facilitate the diffusive supply of silica and release water molecules in proto-crystals of xonotlite. Fig. 6C, for example, illustrates incorporation of water molecule in the coupled defects in Q^3 pair. In the second stage of xonotlite growth the defects in Q^3 sites of the tetrahedral chain are subsequently repaired while the relative concentration of the single and coupled defects is evolved according to the diagram in Fig. 9. We believe that the degree of structural order and deviation from the ideal Ca/Si ratio in xonotlite could be directly related to the amount of defects in Q^3 tetrahedra.

According to the conditions of synthesis the systems does not contain other cations then Ca and Si. Therefore we assumed that the charge compensation in the defects is fulfilled through the incorporation of OH groups. In natural systems and industrial poly-phase cements the chemistry is more diverse and other cations can play a charge compensating role. The defects sites are therefore the primary candidates for incorporation of foreign ions into the xonotlite structure.

Similar to the xonotlite, 11.3 Å tobermorite also contains bridging Q^3 and "paired" Q^2 sites. On a speculative manner we can use the results obtained for xonotlite to discuss the structure of tetrahedral chains in tobermorite and C–S–H phases. We suggest that short silica chains, which consist of mainly "paired" Q^2 silica tetrahedra, are initially formed in C–S–H phases. The

increase of the Si content in cement phases corresponds to "repairing" missing Q^3-like sites which give rise to extension of the silica chain. Indeed, a number of experimentally based models for C–S–H phases [35–37] assume omission of bridging tetrahedra and subsequent polymerisation of the silica chain. Depending on the Ca/Si ration the Ca ions play a charge compensating role bridging isolated Q^2 pairs. All these concepts are well in agreement with preferential stability of defects in Q^3 sites of xonotlite chain observed in this work. It should be noted, however, that other factors like Al content for example play an important role in the formation of C–S–H phases and tobermorite [38]. Further studies are necessary to reveal the relative importance of charge compensation mechanisms, the isomorphic substitutions and polymerisation of the silicate chain on the structure of C–S–H phases.

4.2. Interpretation of the IR spectra

Idealized xonotlite only contains hydrogen in the form of O10–H...O2 groups. The natural and synthetic samples indicate presence of at least two types of OH groups [3] and traces of molecular water. The IR spectral of the synthetic xonotlite contains a broad absorption band in the 3200–3500 cm^{-1} range (Fig. 5A). This band is most probably produced by stretching of the different OH groups forming strong hydrogen bonds in defects of the silicate double chain, the water molecules at the surface and possibly some traces of structurally incorporated molecular water. As described in the Section 3.4, we were not able to produce the samples without surface absorbed water. Therefore an unambiguous identification of absorption bands, caused by the structurally incorporated OH groups in the measured spectra (apart from O10–H band) was not possible. The theoretical calculations also have limitations, which make the comparison of the experimental and the simulated IR spectra difficult. Unlike the measurements the calculated spectra does not contain contribution from any kind of surface absorbed water, which allows identification of the OH bands in defects. Due to the small size of the simulated cell, however, the concentration of defects in the simulation is much higher than in the synthetic samples, which explains the high intensity of the defect associated OH vibrations compared to O10H band (Fig. 5C). Additionally, the defects cause significant broadening of O10H band. One may expect that in larger simulation cell the absorption bands characteristic to OH groups in defects will be shifted toward the O10H frequency because of additional relaxation in the structure.

Based on the simulations the sharp absorption band at 3620 cm^{-1} can be unambiguously assigned to the O10H group. The calculated absorption bands for O9H, O5H and O6H groups in the Q^3 defect tetrahedra coincide with the frequency range of the broad absorption band in the measured spectra at 3200–3500 cm^{-1}, but can not be identified as single bands, due to above mentioned limitations of both the modelling and experimental data. At the present time, we are not able to distinguish between contributions from structurally incorporated OH groups and the surface absorbed water. Further theoretical and experimental investigations are necessary to distinguish the various contributions to the absorption band in the given frequency range.

5. Conclusions

Our investigation of the xonotlite synthesis product is in agreement with previous studies [1]. Deviation of the calcium/silica ratio from the unity, which was observed after 30 days of hydrothermal synthesis, is likely due to disorder in the structure and Si defects. The results of the Rietveld refinement show, that the xonotlite polytype M2a2bc is the dominant phase under the given reaction conditions. The structure of hydrogen bond and stretching modes of OH groups in M2a2bc polytype was investigated by means of ab initio simulations. The Si deficiency in the natural and synthetic samples is explained by formation of the defects in tetrahedral silicate chain. The simulations predict that the missing tetrahedra in Q^3 sites entirely dominate over defects in Q^2 sites. Moreover, the paired substitutions in neighbouring Q^3 sites are energetically more stable than isolated Q^3 defects. Thus, despite the entropy effect, the coupled Q^3 substitution becomes dominant already at small concentrations of tetrahedral defects. Such defects provide the necessary space for possible incorporation of foreign ions and water in the structure of xonotlite. In the present calculations the charge compensation on the defects was fulfilled by inclusion of additional OH groups. The vibrational frequencies of OH groups in defects are red shifted relative to O10H bands.

Acknowledgments

The calculations were performed on the CRAY-XT3 cluster at the CSCS Manno. We thank Dr. Erich Wieland for the helpful comments during the experiments and the comments on earlier version of this paper. Dr. F. Winnefeld (EMPA, Switzerland) provided measuring time and experimental assistance with the XRD measurements and his contribution to this project is gratefully acknowledged. Thanks are extended to D. Kunz, R. Brütsch, A. Frei and Dr. R. Koetz (PSI) for assistance during the wet chemistry experiments, SEM, TG/DTA and IR investigations. Prof. B. Wehrli (EAWAG, Switzerland) is gratefully acknowledged for constructive comments and discussions. Partial financial support was provided by the National Cooperative for the Disposal of Radioactive Waste (Nagra), Switzerland.

Appendix A

Quantitative phase identification and Rietveld refinements. According to the Rietveld method the crystal structure parameters are obtained by least-square fit of the powder diffraction pattern. The intensities y_{ci} of each phase are determined from the structure factor, $|F_k|^2$, which is calculated from the structure model by summing up the calculated contributions from neighbouring Bragg reflections plus the background (Eq. (A1)):

$$y_{ci} = S_i \sum_k L_k |F_k|^2 \varphi(2\theta_i - 2\theta_k) P_k A + y_{bi}, \quad \text{(A1)}$$

where S_i is the scaling factor of phase i, k represents the Miller indices (h k l) for a Bragg reflection, L_k contains the Lorenz polarization and multiplicity factors, φ is the reflection profile function, P_k is the preferred orientation function, A is the absorption factor, F_k is the structure factor for the k^{th} Bragg reflection and y_{bi} is the background intensity [39]. The factor minimized in the least-square refinement is the residual, S_y, calculated in the case of constant wavelength angle-dispersive data by Eq. (A2):

$$S_y = \sum_i w_i (y - y_{ci})^2, \tag{A2}$$

where $w_i = 1/y_{ci}$, y is the observed intensity and y_{ci} is the calculated intensity [39].

In the quantitative phase analysis using the Rietveld method, the weight fraction w_i of each crystalline component in the mixture is calculated from the corresponding scaling factor S_i for that phase and the unit mass (M_i) and volume (V_i) by Eq. (A3):

$$w_i = \frac{S_i M_i V_i}{\sum_j S_j M_j V_j}, \tag{A3}$$

where

$$\sum_i w_i = 1.0, \tag{A4}$$

In this work the Rietveld refinement was performed using the GSAS package [40] and the graphical user interface (GUI) editor for GSAS experiment [41].

As starting models for the quantitative characterization of the samples, the four known xonotlite polytypes M2a2bc, Ma2bc, M2a2b2c and Ma2b2c [42], with the space groups P-1, P 2/a, A-1 and A2/a, respectively are used. The Ca, Si and O atoms are ordered into positions 1h, 1f and 2i (Ca), 1i (Si and O) of P-1, 2i of A-1, 2e of P2/a as well 4c of A 2/a [2].

The whole powder diffraction pattern of synthetic xonotlite including the region from 5.008–79.978 ($2\theta°$) was refined and yielded an agreement index chi^2 of 1.479 for 15 variables. The background was fitted using the shifted Chebyshev function with 24 background coefficients. As the complexity of the pattern did not allow background subtraction, the background was refined as proposed by McCusker and co-workers [43]. The profiles were modelled using Simpson's rule integration of a pseudo-Voigt function (function 2) [44,45]. The Rp, wRp, and R (F^2) values were determined to be 3.01, 4.14, and 6.76, respectively. The weighted Durbin-Watson d value [46–48] was estimated to be 0.74.

Whenever amorphous phases exist in the system, the scattering contribution of the amorphous phase is part of the background and thus not included in Eq. (A4). The fraction of the amorphous phase can be calculated using the internal standard method, where a known fraction of standard powder (for instance: corundum or quartz) is added to the sample and treated as a component of the sample. After finishing of the Rietveld refinement, the refined phase fractions are converted into weight fractions and rescaled by the ratio between refined (x_{sc}) and the known (x_s) amount of added standard. The percentage of the amorphous phase x_a in the sample can be calculated directly from the weight of the internal standard according to Eq. (A5) [49]:

$$x_a = \frac{100}{(100 - x_s)} \left(1 - \frac{x_s}{x_{sc}}\right), \tag{A5}$$

To estimate the amorphous content in xonotlite, a data set from a xonotlite sample with pure quartz added as internal standard (10%) was collected. The quartz intensities were corrected for a preferred orientation effect along the [101] direction using the March-Dollase formalism [50].

References

[1] G.L. Kalousek, T. Mitsuda, H.F.W. Taylor, Xonotlite: Cell parameters, thermogravimetry and analytical electron microscopy, Cement and Concrete Research 7 (3) (1977) 305–312.

[2] C. Hejny, T. Armbruster, Polytypism in xonotlite $Ca_6Si_6O_{17}(OH)_2$, Zeitschrift für Kristallographie 216 (2001) 396–408.

[3] H. Noma, Y. Adachi, Y. Matsuda, T. Yokoyama, ^{29}Si and ^{1}H NMR of natural and synthetic xonotlite, Chemistry Letters (3) (1998) 219–220.

[4] M.R. Hansen, H.J. Jakobsen, J. Skibsted, ^{29}Si chemical shift anisotropies in calcium silicates from high-field ^{29}Si MAS NMR spectroscopy, Inorganic Chemistry 42 (7) (2003) 2368–2377.

[5] X. Cong, R.J. Kirkpatrick, ^{29}Si MAS NMR study of the structure of calcium silicate hydrate, Advanced Cement Based Materials 3 (3–4) (1996) 144–156.

[6] X. Cong, R.J. Kirkpatrick, ^{29}Si and ^{17}O NMR investigation of the structure of some crystalline calcium silicate hydrates, Advanced Cement Based Materials 3 (3–4) (1996) 133–143.

[7] K. Garbev, Forschungszentrum Karlsruhe - Wissenschaftliche Berichte - FZKA 6877, 2004, pp. 1–215.

[8] S. Shaw, S.M. Clark, C.M.B. Henderson, Hydrothermal formation of the calcium silicate hydrates, tobermorite ($Ca_5Si_6O_{16}(OH)_2.4H_2O$) and xonotlite ($Ca_6Si_6O_{17}(OH)_2$): an in situ synchrotron study, Chemical Geology 167 (1–2) (2000) 129–140.

[9] R. Kirkpatrick, A.G. Kalinichev, X. Hou, L. Struble, Experimental and molecular dynamics modeling studies of interlayer swelling: water in kanemite and ASR gel, Materials and Structures/Concrete Science and Engineering 38 (2005) 449–458.

[10] P. Faucon, J.M. Delaye, J. Virlet, J.F. Jacquinot, F. Adenot, Study of the structural properties of the C–S–H(I) by molecular dynamics simulation, Cement and Concrete Research 27 (10) (1997) 1581–1590.

[11] A.G. Kalinichev, J. Wang, R.J. Kirkpatrick, Molecular dynamics modeling of the structure, dynamics and energetics of mineral–water interfaces: application to cement materials, Cement and Concrete Research 37 (3) (2007) 337–347.

[12] A.G. Kalinichev, R.J. Kirkpatrick, Molecular Dynamics Modeling of Chloride Binding to the Surfaces of Calcium Hydroxide, Hydrated Calcium Aluminate, and Calcium Silicate Phases, Chemistry of Materials 14 (8) (2002) 3539–3549.

[13] I.S. Bell, P.V. Coveney, Molecular modelling of the mechanism of action of borate retarders on hydrating cements at high temperature, Molecular Simulation 20 (1997) 331–356.

[14] P.V. Coveney, W. Humphries, Molecular modelling of the mechanism of action of phosphonate retarders on hydrating cements, Journal of the Chemical Society. Faraday Transactions 92 (1996) 831–841.

[15] M.C. Payne, M.P. Teter, D.C. Alan, T.A. Arias, J.D. Joannopoulos, Iterative minimization techniques for abinitio total-energy calculations — dynamics and conjugate gradients, Reviews of Modern Physics 64 (1992) 1045–1097.

[16] P. Hohenberg, W. Kohn, Inhomogeneous electron gas, Physical Review 136 (3B) (1964) 864–871.

[17] W. Kohn, L.J. Sham, Self-consistent equation including exchange and correlation effects, Physical Review 140 (4A) (1965) A1133–A1138.

[18] CPMD v 3.9 In Copyright IBM Corp 1990–2004, Copyright MPI fuer Festkoerperforschung Stuttgart 1997–2001.
[19] A.D. Becke, Density-functional exchange-energy approximation with correct asymptotic behavior, Physical Review A 38 (6) (1988) 3098–3100.
[20] C. Lee, W. Yang, R.G. Parr, Development of the Colle-Salvetti correlation-energy formula into a functional of the electron density, Physical Review B 37 (2) (1988) 785–789.
[21] N. Troullier, J.L. Martins, Efficient pseudopotentials for plane-wave calculations, Physical Review B 43 (1991) 1993–2006.
[22] S.V. Churakov, M. Iannuzzi, M. Parrinello, Ab Initio study of dehydroxylation-carbonation reaction on brucite surface, Journal of Physical Chemistry B 108 (31) (2004) 11567–11574.
[23] R. Car, M. Parrinello, Unified approach for molecular dynamics and density-functional theory, Physical Review Letters 55 (22) (1985) 2471–2474.
[24] P.L. Silvestrelli, M. Bernasconi, M. Parrinello, Ab initio infrared spectrum of liquid water, Chemical Physics Letters 277 (1997) 478–482.
[25] W. Press, H. Flannery, B.P. Teukolsky, W.T. Vetterling, Numerical Recipes in FORTRAN 77: The Art of Scientific Computing, Cambridge University Press, 1992.
[26] P.E. Blöchl, M. Parrinello, Adiabaticity in first-principles molecular dynamics, Physical Review B 45 (16) (1992) 9413–9416.
[27] H.J. Monkhorst, J.D. Pack, Special points for Brillouin-zone integrations, Physical Review B 13 (12) (1976) 5188–5192.
[28] M. Iannuzzi, M. Parrinello, Efficient k×p method for the calculation of total energy and electronic density of states, Physical Review B 64 (23) (2001) 233104–233108.
[29] I.D. Brown, The Chemical Bond in Inorganic Chemistry — The Bond Valence Model, Oxford University Press, 2002.
[30] I.D. Brown, D. Altermatt, Bond-valence parameters obtained from a systematic analysis of the Inorganic Crystal Structure Database, Acta Crystallographica. Section B 41 (4) (1985) 244–247.
[31] F.A. Kröger, The Chemistry of Imperfect Crystals, North-Holland, Amsterdam, 1974.
[32] N.B. Singh, S. Rai, N. Singh, Highly reactive β-dicalcium silicate, Journal of the American Ceramic Society 85 (2002) 2171–2176.
[33] J.J. Thomas, J.J. Chen, A.J. Allen, H.M. Jennings, Effects of decalcification on the microstructure and surface area of cement and tricalcium silicate pastes, Cement and Concrete Research 34 (12) (2004) 2297–2307.
[34] D.R. Moorehead, E.R. McCartney, Hydrothermal formation of calcium silicate hydrates, Journal of the American Ceramic Society 48 (11) (1965) 565–569.
[35] I.G. Richardson, The nature of C–S–H in hardened cements, Cement and Concrete Research 29 (8) (1999) 1131–1147.
[36] I.G. Richardson, Tobermorite/jennite- and tobermorite/calcium hydroxide-based models for the structure of C–S–H: applicability to hardened pastes of tricalcium silicate, [beta]-dicalcium silicate, Portland cement, and blends of Portland cement with blast-furnace slag, metakaolin, or silica fume, Cement and Concrete Research 34 (9) (2004) 1733–1777.
[37] H.F.W. Taylor, Proposed structure for calcium silicate hydrate gel, Journal of the American Ceramic Society 69 (1986) 464–467.
[38] G.K. Sun, J.F. Young, R.J. Kirkpatrick, The role of Al in C–S–H: NMR, XRD, and compositional results for precipitated samples, Cement and Concrete Research 36 (1) (2006) 18–29.
[39] R.A. Young, The Rietveld Method, Oxford University Press, 1993.
[40] A.C. Larson, R.B. Von Dreele, GSAS, General Structure Analysis System, Report MS H805, Los Alamos National Laboratory, 1994.
[41] B.H. Toby, EXPGUI, a graphical user interface for GSAS, Journal of Applied Crystallography 34 (2001) 210–213.
[42] J.A. Gard, A system of nomenclature for the fibrous calcium silicates, and a study of xonotlite polytypes, Nature 211 (5053) (1966) 1078–1079.
[43] L.B. McCusker, R.B. Von Dreele, D.E. Cox, D. Louër, P. Scardi, Rietveld refinement guidelines, Journal of Applied Crystallography 32 (1999) 36–50.
[44] P. Thompson, D.E. Cox, J.B. Hastings, Rietveld refinement of Debye-Scherrer synchrotron X-ray data from Al_2O_3, Journal of Applied Crystallography 20 (1987) 79–83.
[45] C. Howard, The approximation of asymmetric neutron powder diffraction peaks by sums of Gaussians, Journal of Applied Crystallography 15 (6) (1982) 615–620.
[46] J. Durbin, G.S. Watson, Testing for serial correlation in least squares regression I, Biometrika 37 (3–4) (1950) 409–428.
[47] J. Durbin, G.S. Watson, Testing for serial correlation in least squares regression II, Biometrika 38 (1–2) (1951) 159–178.
[48] J. Durbin, G.S. Watson, Testing for serial correlation in least squares regression III, Biometrika 58 (1) (1971) 1–19.
[49] A.F. Gualtieri, G. Brignoli, Rapid and accurate quantitative phase analysis using a fast detector: quantitative phase analysis, Journal of Applied Crystallography 37 (2004) 8–13.
[50] W. Dollase, Correction of intensities for preferred orientation in powder diffractometry: application of the March model, Journal of Applied Crystallography 19 (4) (1986) 267–272.